

---

# NeMO: Neural Map Growing System for Spatiotemporal Fusion in Bird’s-Eye-View and BDD-Map Benchmark

---

Xi Zhu\* Xiya Cao\* Zhiwei Dong Caifa Zhou Qiangbo Liu Wei Li Yongliang Wang†  
Riemann Lab, 2012 Laboratory,  
Huawei Technologies Co. Ltd

## Abstract

Vision-centric Bird’s-Eye View (BEV) representation is essential for autonomous driving systems (ADS). Multi-frame temporal fusion which leverages historical information has been demonstrated to provide more comprehensive perception results. While most research focuses on ego-centric maps of fixed settings, long-range local map generation remains less explored. This work outlines a new paradigm, named NeMO, for generating local maps through the utilization of a readable and writable big map, a learning-based fusion module, and an interaction mechanism between the two. With an assumption that the feature distribution of all BEV grids follows an identical pattern, we adopt a shared-weight neural network for all grids to update the big map. This paradigm supports the fusion of longer time series and the generation of long-range BEV local maps. Furthermore, we release BDD-Map, a BDD100K-based dataset incorporating map element annotations, including lane lines, boundaries, and pedestrian crossing. Experiments on the NuScenes and BDD-Map datasets demonstrate that NeMO outperforms state-of-the-art map segmentation methods. We also provide a new scene-level BEV map evaluation setting along with the corresponding baseline for a more comprehensive comparison.

## 1 Introduction

In the realm of autonomous driving, the ability to perceive and comprehend the surrounding environment is of utmost importance. The Bird’s-Eye-View (BEV) representation is particularly desirable for its ability to accurately display the spatial placement of objects and road elements in a three-dimensional space [36, 21, 5, 17, 41, 3]. Many vision-based Bird’s-Eye-View (BEV) studies perception [2, 19, 30, 15, 26, 12] have shown significant progress in recent years.

Besides utilizing multi-view information[19, 15], vision-based Bird’s-Eye-View (BEV) perception also taps into the potential of time-series images. Leveraging time-series data can effectively address challenges such as visual occlusion and visual illusions, particularly for static elements, like road elements. Researchers have explored temporal fusion via warping or query-based approaches[16, 22, 28, 40, 20], demonstrating that temporal fusion improves perception in challenging environments such as occluded circumstances. However, these works limit to ego-centric environment and do not consider the global perception of the environment corresponding to the traveled distance.

In this paper, we present a Neural Map grOWing system, **NeMO**, that can digest image sequences, unravel the details of a journey, and produce a comprehensive long-range local map of the environment.

---

\*Equal contribution.

†Corresponding author. Email: wangyongliang775@huawei.com

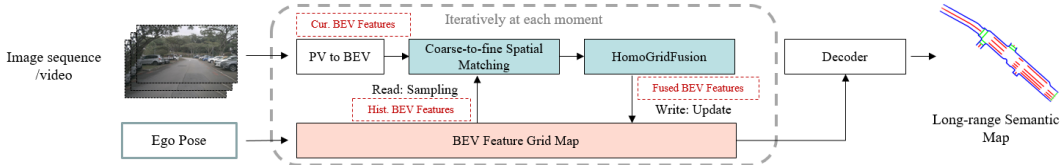


Figure 1: NeMO system overview.

Long-range local map is an important input for downstream modules, such as map matching and navigation. In comparison with the BEV maps generated with existing methods, a long-range local map usually has a larger spatial area, requiring fusion of more frames.

Expanding the spatial size of the BEV plane using current state-of-the-art spatio-temporal fusion methods[20, 28] can be a straightforward approach. However, it is not practical or easily extendable because increased computational costs accompany the expansion of the local map. In [19], an alternative approach is proposed where BEV feature maps for related frames are generated and then aligned onto a fixed BEV space based on ego poses to create a local map, followed by max-pooling for overlapping areas. While this approach is universal and is able to fuse any number of frames, two issues still remain unsettled. First, max-pooling may not eliminate false detections and its performance could suffer if the BEV perception results are poor. The second issue is that accuracy of this approach depends on precise ego poses.

To address these issues, NeMO utilizes a BEV-grid-based local map generation paradigm to fuse frames and construct a long-range local map simultaneously. In NeMO, we create a readable and writable BEV feature grid map for feature storage and extraction, a coarse-to-fine spatial matching module to sample and match features in BEV at different timestamp, along with a homogenous grid fusion network to identify and preserve the most valuable features. The read- and writ-able BEV feature grid map (referred to as “the big feature map” in this paper) represents a wider ranged area and stores BEV features, enabling extraction and updating of historical BEV grids whenever required. The system works by initially retrieving BEV features from the current frame. Concurrently, a coarse matching method, is used to sample historical BEV features from the big feature map. To enhance the matching of current and historical features, a finer local spatial matching process is performed. Assuming complete descriptors are present in independent grids, we design a homogeneous grid fusion network to merge the grid-based features. Finally, the corresponding portion of grids in the big feature map is updated with the new fused features. The matching and fusion operations interact in real-time with the big feature map, resulting in an iterative process that enables continuous growth of the neural map. The proposed paradigm offers several advantages. First, it enables the generation of long-range local maps from an arbitrary number of frames at a small and consistent computational cost. Features maintained in the big map integrate all previous information rather than a fixed number of frames. The grid-based coarse-to-fine spatial matching technique mitigates the impact of pose noise, resulting in improved accuracy. The homogenous grid fusion is able to capture, enhance, and update critical information within a grid effectively. It is worth mentioning that NeMO can accommodate a broad spectrum of inputs as it is compatible with any BEV features. A concurrent work<sup>3</sup> NMP[37] proposes a similar approach like NeMO for better online BEV inference with global map as prior information storage, and we provide a brief comparison in Section 2.

We validate NeMO system on NuScenes [4] and BDD100K [39] datasets. Notably, the latter was acquired using smartphones with reduced accuracy in pose information. To supplement the BDD100K dataset with BEV annotations, we provide annotation tools and use the same annotation style as NuScenes [4] for three categories (lane line, pedestrian crossing, and boundary). The annotated dataset, named BDD-Map, consists of 446 scenes and 426,476 frames.

Our approach demonstrates exceptional performance in the NuScenes dataset, significantly improve performance of HDMapNet [19] by a large margin. Additionally, our approach shows greater accuracy than the current state-of-the-art temporal BEV perception method BEVerse [40], highlighting the flexibility and effectiveness of our system. Furthermore, we provide a benchmark for scene-level local map generation for both datasets.

<sup>3</sup>The first version of the current work was submitted to NeurIPS on 2023-05-17. Shortly after that, we became aware of Xiong et al.[37] CVPR submission which was posted on arxiv on 2023-04-17.

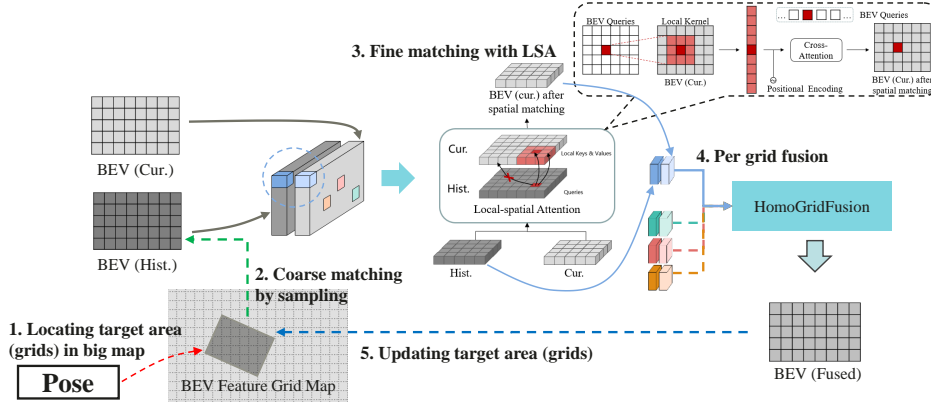


Figure 2: Coarse-to-fine spatial matching and HomoGridFusion models.

## 2 Related Work

**BEV lane segmentation map construction.** The conversion of static road elements in Perspective View (PV) to Bird’s-Eye-View (BEV) can be broadly classified into geometry-based and learning-based approaches. The former utilizes the physical principles underlying the geometric projection relationship between Perspective View (PV) and Bird’s-Eye-View (BEV), while the latter employs data-driven approaches that involve the use of learnable neural networks for mapping. The pioneering geometry-based approach is homography-based IPM (Inverse Perspective Mapping [24]), which inversely maps PV information onto BEV plane utilizing homography matrices with flat-ground assumption [9, 30, 9, 25, 6]. Therefore, IPM-like methods may have unsatisfactory performance when the ground is not flat. Another geometry-based way, represented by Lift, Splat, and Shoot (LSS) [27], is to lift 2D pixels to 3D space via depth prediction [32, 11, 29, 40]. Learning-based methodologies have made great progress in recent years [23, 31, 13, 38, 19, 20, 22, 34, 35]. HDMaNet [19] utilizes MLP to cover complex transformation between PV and BEV features. Transformers with BEV queries, first used by Tesla [1] for multi-view PV-BEV transformation, have gained their popularity in recent works [7, 20, 22, 26, 10] because of the superior efficacy. In this approach, view transformation is usually conducted using cross-attention between PV features and BEV queries with positional encoding [20]. As this dense-query design leads to memory cost issue in the cross-attention operation, several studies such as BEVSegFormer [26], PersFormer [7], and BEVFormer [20] deploy deformable attention [42] for faster computation. Concurrently, GKT [8] leverages camera’s parameters to find 2D reference points such that queries can focus on small regions.

**Temporal fusion in BEV lane segmentation.** Existing studies have confirmed that utilizing multi-frame information helps to improve detection accuracy while alleviating occlusion issue in single frame perception [20, 22, 40, 28]. BEVerse [40] and BEVFormer [20] wrap past BEV features to the present frame with ego motion information, while the former mainly creates temporal block stack and deploys 3D convolutions, and the latter utilizes self-attention layer to query wrapped previous BEV features with current BEV features. Differently, [22] and [28] directly query PV features. PETRv2 [22] combines temporal information by adding coresponding positional encoding for both previous and current image features. Specifically, it generates previous frame’s positional encoding by converting its 3D coordinates to the current one according to ego motion, and concatenate the converted 3D coordinates to the 2D features to obtain 3D position-aware features. 3D position-aware features of different frames can be further queried by BEV queries. Unifusion [28] treats temporal fusion as a multi-view fusion problem by converting past frames to virtual views which are transformed to the ego BEV space with view transformation. The multi-view features are then fused with BEV queries in cross-attention layer.

Multi-frame fusion is also an inevitable part for long-range local map generation in ADS. Unifusion [28] proposes new BEV settings representing larger areas for longer series temporal fusion. However, adopting larger settings has to strike a balance between BEV grid resolution and computational complexity, which may not only impact the result accuracy but also impose constraints on the map size. A scene-level long-term temporal fusion method proposed by HDMaNet [19] is to paste BEV

maps of previous frames into current’s with ego pose and fuse the overlapped grids via max pooling. Yet, fusion methods like temporal max pooling may unexpectedly retain noise thus do not perform stably in different scenes. The real-time long-range local map generation logic proposed by Tesla [1] is to update only a portion of BEV grids in a long-range map at each moment with “spatial RNN”. Our work delves further into this logic by proposing a practical pipeline and solution with the aim of aiding future researchers in their exploration of this field.

Most similar to our approach and developed in parallel is NMP [37], which leverages a city-wide global map for feature prior storage, and a current-to-prior attention followed by ConvGRU module for prior and current feature fusion for online inference. A main difference is that we use a shared recurrent neural network for homogeneous grid fusion, with an assumption that all grid features have identical data distribution pattern regardless of the grid’s position in local BEV plane. Besides, we adopt local spatial attention for fine matching, which further reduces the computation cost in online inference process. Moreover, our HDMaPNet-based NeMO outperforms [37] in NuScenes dataset for local BEV, and we provide a benchmark for scene-level long-range map generation.

### 3 Methodology

The proposed NeMO system generates a long-range semantic map using image sequence and ego pose information as inputs, as depicted in Figure 1. At each time step, the image  $\mathcal{I}_{cur}$  is fed into a PV-to-BEV neural network, which produces BEV features  $\mathcal{F}_{cur}^{bev}$  that are relative to the ego vehicle. The historical BEV features  $\mathcal{F}_{hist}^{bev}$  that correspond to the same area are retrieved from the BEV Feature Grid Map (also known as “the big feature map”) through a “coarse-to-fine” spatial matching technique, which we refer to as “reading”. The BEV features  $\mathcal{F}_{cur}^{bev}$  and  $\mathcal{F}_{hist}^{bev}$  are then integrated in the HomoGridFusion model to generate  $\mathcal{F}_{fused}^{bev}$ , and “written” back to the big feature map using the ego pose  $E_{cur}$  associated with current moment, which updates the corresponding grids. Finally, the updated big feature map is fed into a decoder to generate the desired local long-range semantic map.

**PV-to-BEV revisiting.** Many studies focus on PV-to-BEV transformation [19, 20, 30, 15, 40], which involves converting images  $\mathcal{I}_{cur}$  to BEV features  $\mathcal{F}_{cur}^{bev} \subseteq \mathbb{R}_{O_e}^{H_{bev} \times W_{bev} \times K}$  in ego coordinates  $O_e$ , where  $H_{bev}$  and  $W_{bev}$  represent the height and width of the BEV plane (i.e., number of grids along height and width), and  $K$  is feature dimension. Here the input  $\mathcal{I}_{cur}$  can be either one front-view image or multiple images from surrounding cameras. While some research looked into ways to improve ego-centric BEV perception by integrating multiple timestamp frames [20, 40], ultimately they still produce one single-frame BEV perception map. NeMO is compatible with any PV-to-BEV frontend as long as it can produce a BEV feature map  $\mathcal{F}_{cur}^{bev}$  for current timestamp.

#### 3.1 Coarse-to-fine spatial matching

NeMO system employs a two-stage “coarse-to-fine” spatial matching to obtain historical BEV features  $\mathcal{F}_{hist}^{bev} \subseteq \mathbb{R}_{O_e}^{H_{bev} \times W_{bev} \times K}$  that correspond to the same spatial area as the  $\mathcal{F}_{cur}^{bev}$ .

We first use coordinate transformation to obtain a “coarse” position for historical BEV features in the readable and writable big feature map  $\mathcal{F}^{map} \subseteq \mathbb{R}_{O_g}^{H_{map} \times W_{map} \times K}$ , which is in a scene global coordinate system  $O_g$ . The size of  $\mathcal{F}^{map}$ , with dimensions  $H_{map} \times W_{map}$ , is much larger than that of the BEV plane  $H_{bev} \times W_{bev}$ . The ego pose  $E_{cur}$  is critical in identifying the optimal target region within the big feature map for retrieving the historical BEV information. Define grid coordinates in ego-centric BEV plane as  $C_{bev}$ , their coordinates in the big feature map is coarsely determined as  $C_{map} = E_{cur} C_{bev}$ . The  $C_{map}$  coordinates serve as reference points to sample  $\mathcal{F}_{hist}^{bev}$  from  $\mathcal{F}^{map}$ .

In contrast to established techniques that save previous frames’ features and wrap it to current moment’s coordinate system, potentially leading to loss of information, the coarse spatial matching approach introduced in this study, which employs the big feature map, seamlessly attains spatial alignment for both past and present features with shared scale on the BEV grid plane. Moreover, the big map range ( $H_{map}$  and  $W_{map}$ ) is adjustable and can be expanded on demand over time.

In ideal situations when  $E_{cur}$  is accurate and the grid resolution is high,  $\mathcal{F}_{cur}^{bev}$  and  $\mathcal{F}_{hist}^{bev}$  are perfectly spatially aligned. However, this is not always the case as sensors may have noises, and grid density needs to be balanced with computational cost. Therefore, we propose the “fine” spatial matching stage to alleviate the misalignment issue with a grid-based local-spatial attention (LSA) network. The

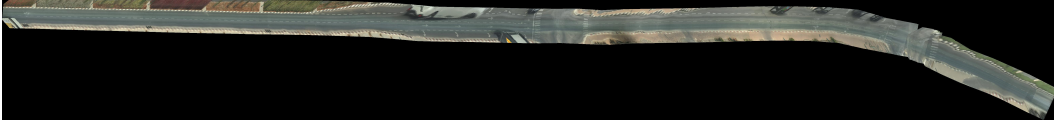


Figure 3: Pixel map in ground plane.

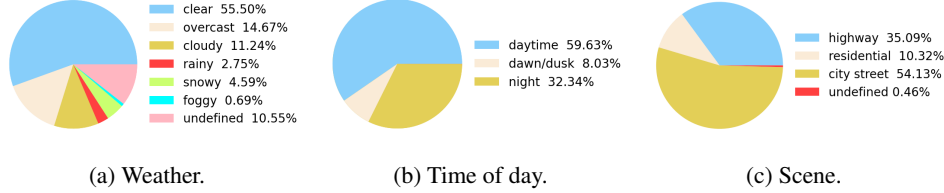


Figure 4: BDD-Map weather condition, time of day, and scene distributions.

LSA model adopts a local querying approach for each grid by considering only its adjacent grids, rather than querying all grids globally, which not only yields more accurate results but also incurs low computational costs. For a grid  $G$  with initialized coarse coordinate  $C_{map}^G$  in the big feature map, we sample features from  $\mathcal{F}_{cur}^{bev}$  using a local kernel that is expanded according to  $C_{map}^G$ , as shown in the upper part of Figure 2. Denote the sampled features as  $\mathcal{F}_{localkernel}^G$ . BEV queries  $Q_{bev}$  are generated by positional encoding in ego-centric BEV plane. Query for  $G$ , denoted as  $Q_{bev}^G$  is determined by its position in BEV plane,  $C_{bev}^G$ . For grid  $G$ , the fine matching current feature is formulated as:

$$\bar{\mathcal{F}}_{cur}^{bev,G} = CA(Q_{bev}^G, \mathcal{F}_{localkernel}^G)$$

where  $CA$  refers to cross-attention. With a query-based structure to integrate information from local regions for each BEV grid, we get  $\bar{\mathcal{F}}_{cur}^{bev} \subseteq \mathbb{R}_{O_e}^{H_{bev} \times W_{bev} \times K}$  that better aligned  $\mathcal{F}_{hist}^{bev}$ .

### 3.2 HomoGridFusion

$\bar{\mathcal{F}}_{cur}^{bev}$  and  $\mathcal{F}_{hist}^{bev}$  is combined with HomoGridFusion, which is a per-grid temporal fusion model of current-historical features. The core spirit of HomoGridFusion is the grid-based shared recurrent network structure. The current and historical BEV features  $\bar{\mathcal{F}}_{cur}^{bev}$  and  $\mathcal{F}_{hist}^{bev} \subseteq \mathbb{R}_{O_e}^{H_{bev} \times W_{bev} \times K}$  represent the same area with the same scale, enabling grid-based temporal fusion at this step. For each grid  $G$  with coordinate  $(h, w)$  in BEV plane, where  $h \in \{1, 2, \dots, H_{bev}\}$  and  $w \in \{1, 2, \dots, W_{bev}\}$ , we can get current BEV feature  $\bar{\mathcal{F}}_{cur}^{bev}[h][w]$  and corresponding historical BEV feature  $\mathcal{F}_{hist}^{bev}[h][w]$ , both of which are  $K$ -dimensional feature vectors. They are integrated into a new  $K$ -dimensional feature vectors in a recurrent manner, that  $\mathcal{F}_{hist}^{bev}[h][w]$  is treated as a hidden state and  $\bar{\mathcal{F}}_{cur}^{bev}[h][w]$  is a new observation, and we get the new fused state  $\mathcal{F}_{fused}^{bev}[h][w]$  with a recurrent model. Since all grids share a same recurrent model, it is easy to parallel in that the BEV feature arrays are unfolded to form a  $H_{bev} \times W_{bev}$  sized batch. This design rests on the assumption that the feature distribution of all BEV grids follows identical pattern, notwithstanding the grid's spatial position  $(h, w)$  on the BEV plane  $\mathbb{R}_{O_e}^{H_{bev} \times W_{bev} \times K}$ .  $\bar{\mathcal{F}}_{cur}^{bev}$  and  $\mathcal{F}_{hist}^{bev}$  are embedded in the ego coordinate system which moves as the vehicle advances.  $\bar{\mathcal{F}}_{cur}^{bev}$  represents the features of a specific are based on a single observation, whereas  $\mathcal{F}_{hist}^{bev}$  is based on historical observations. The assumption is that the method of combining these two types of features should be the same across different areas regardless of spatial properties.

The main body of the HomoGridFusion model presented in this paper is a two-block bidirectional recurrent network, each followed by an Multi-layer Perceptron (MLP) layer. Prior to the recurrent network blocks, we add three convolutional layers to  $\bar{\mathcal{F}}_{cur}^{bev}$  and  $\bar{\mathcal{F}}_{hist}^{bev}$  to better capture visual pattern for each grid.

## 4 BDD-Map Dataset

BDD100K is a large-scale diverse driving video dataset that covers a wide range of driving scenarios, including different times of day and weather conditions in multiple cities. Different from other

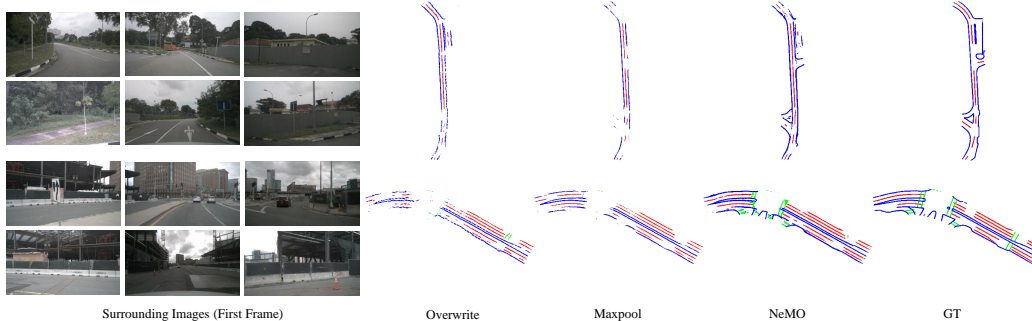


Figure 5: Visual comparison on NuScenes scene-level long-range map generation.

popular autonomous driving dataset such as NuScenes, Argoverse 2 and Waymo, BDD100K provides less accurate ego motions due to hardware limitation. Instead of using Lidar, BDD100K employs GPS/IMU information from phones to generate rough trajectories. All smartphones are equipped with cameras, GPS and IMU. Therefore, BDD100K represents the most universal perception system for all customers and covers much richer scenes. The computer vision community has greatly benefited from the extensive BDD100K driving scene data. However, its primary usage is for object detection, scene segmentation, and behavior prediction. Few people use it for road structure perception to provide reliable maps. In this work, we attempt to utilize a small portion of it to do semantic map perception task. Although the constructed map accuracy is limited by trajectories precision, they exhibit approximate road topology structure that are sufficient to support lane-level localization and augmented reality road guidance.

Generating road elements annotations such as lanes, boundaries and pedestrian crossings for a BDD clip in BEV is a challenging task. BDD100K only offers one frame lane annotations per entire clip, leaving out annotations for the majority frames within the clip. Additionally, the dataset does not officially provide extrinsic and intrinsic parameters for each clip, further hindering the process. To tackle these challenges, we develop a semi-automated road elements annotation system. Considering the static nature of road elements and their better observability in a BEV, we propose to convert each 40s video clip into a single large frame as a pixel map as show in figure 1 (a). The pixel map effectively displays all road elements, and obscured areas due to dynamic objects such as cars can be easily annotated with the help of surrounding elements. We provide more details about the semi-automatic annotation pipeline in Appendix A.2.

There are 100 sets in BDD100K and each contains 1000 clips. We randomly selected set 66 and ran the annotation pipeline, resulting in 446 valid ground-plane pixel map with complete road element annotations in BEV and reasonable camera parameters. We omitted the remaining portion due to an unreasonable trajectory or the inability to estimate a suitable extrinsic matrix. We will release the annotated data as an extension of BDD100K, named BDD-Map. The weather condition, scene, and time of day distributions are shown in Figure 4. Meanwhile, we will release annotation tools since a large portion of BDD100K remains unlabeled and we hope to take advantage of the diversity of BDD100K to promote the development of semantic map perception.

## 5 Experiment

### 5.1 Experimental Settings

**Datasets and tasks.** We conduct experiments on two open datasets, namely NuScenes (“Nus” in the following tables) [4] and aforementioned BDD-Map (“BDD” in the following tables). NuScenes has 1000 scenes. Following HMapNet [19] settings, we use training set (700 scenes) for model training and validation set (150 scenes) for evaluation. BDD-Map has 446 scenes in total, in which 400 scenes are used for training and 46 scenes for evaluation. Regarding the temporal model training, we set frame-per-clip  $T = 4$  and step-size  $D = T = 4$  (the distance between the first frames of two consecutive clips when splitting), splitting NuScenes training set into 6923 clips, and BDD-Map dataset into 9565 clips. Following [19], we focus on semantic map segmentation considering road elements of lane line, pedestrian crossing, and boundary.



Table 1: Experiments of BEV segmentation without and with temporal fusion, for both single front view (*fcam*) and six surrounding image (*6cam*) inputs. Three segmentation classes are road divider (Divider), pedestrian crossing (Ped Xing), and boundary (Boundary). \* means the results are reported in the paper [19, 40]. † means the results are reimplemented in this work.

<i>fcam</i>		#Param.	Temp	mIoU(%)			
				Divider	Ped Xing	Boundary	All
Nus	HMapNet <sub>200×200</sub> †	27.0M		38.4	18.7	35.3	30.8
	NeMO <sub>200×200</sub>		✓	40.9 <sup>+2.5</sup>	23.1 <sup>+4.4</sup>	39.4 <sup>+4.1</sup>	34.5 <sup>+3.7</sup>
	NeMO <sub>256×256</sub>	28.2M	✓	42.8	21.2	40.8	34.9
BDD	HMapNet <sub>200×200</sub> †	23.8M		24.3	7.2	14.3	15.3
	NeMO <sub>200×200</sub>		✓	26.7 <sup>+2.4</sup>	10.1 <sup>+2.9</sup>	17.2 <sup>+2.9</sup>	18.0 <sup>+2.7</sup>
	NeMO <sub>256×256</sub>	25.0M	✓	28.4	8.3	15.4	17.4
<i>6cam</i>							
Nus	HMapNet <sub>200×400</sub> *	78.3M		40.6	18.7	39.5	32.9
	NeMO <sub>200×400</sub>		✓	45.9 <sup>+5.3</sup>	26.9 <sup>+8.2</sup>	46.0 <sup>+6.5</sup>	39.6 <sup>+6.7</sup>
	NeMO <sub>384×384</sub>	79.5M	✓	44.7	22.9	44.5	37.4
	BEVerse-Map <sub>200×400</sub> *	54.8M		53.9	41.0	54.5	49.8
	NeMO <sub>200×400</sub>		✓	57.7 <sup>+3.8</sup>	47.8 <sup>+6.8</sup>	57.6 <sup>+3.1</sup>	54.4 <sup>+4.6</sup>
	NeMO <sub>384×384</sub>	55.5M	✓	57.1	47.0	57.6	53.9

**Experimental settings.** To evaluate NeMO system, we use HMapNet [19] and BEVerse [40] as the baseline methods. They are served as PV-to-BEV module in NeMO as well. We conduct experiments under both single front-view image (*fcam*) and six surrounding images (*6cam*) settings for NuScenes dataset, and *fcam* for BDD-Map dataset.

In PV-to-BEV process, we use 30m × 30m ego plane setting for *fcam* with a 200 × 200 BEV plane and a resolution of 0.15m, while for *6cam* we adopt the same 30m × 60m setting (200 × 400) in [19]. In training process, we prepare a fixed-sized plane for each *T*-frame clip in world coordinate system: 256 × 256 for *fcam* and 384 × 384 for *6cam* (Table 1). In inference process, we generate a big map with all frames in each scene, and evaluate the accuracy of these big maps (Table 2). We use the cross-entropy loss for the semantic segmentation, and Adam optimizer [18] for model training with a learning rate of 1e-03 and weight decay of 1e-07, same with the HMapNet model [19]. We train HMapNet-based NeMO with one NVIDIA GeForce RTX 3090, and BEVerse-based NeMO with eight. Implementation details in both training and inference phases are presented in Appendix A.1.

**Evaluation metric and baseline.** For all settings and the big map condition, mean intersection-over-union (mIoU) is used as the evaluation metric. HMapNet [19] and BEVerse[40] are selected as the baselines for per timestamp BEV perception comparison. A major approach of generating big maps from multiple BEVs is stitching single-frame BEVs with ego poses and integrate the overlapped grids. We select two common non-parameterized methods, overwriting the grids by the information captured in the most recent moment or keeping the maximum (maxpool in temporal dimension), as baselines to compare with our neural network temporal fusion way.

## 5.2 Main Results

Table 1 presents results of BEV segmentation performance before and after fusion with NeMO. To provide ego-centric BEV perception on 200 × 200 or 200 × 400 settings evaluation, features in NeMO are extracted back from the big feature map to the ego-centric plane according to ego pose at each moment. For *fcam*, multi-frame fused NeMO outperforms the baseline, single-frame HMapNet[19], in both NuScenes and BDD-Map datasets. For NuScenes *6cam*, NeMO improve HMapNet mIoU by 20.36%, from 32.9 to 39.6. This suggests that the proposed strategy NeMO successfully enhances perception in map growing process by integrating temporal information in consecutive frames. For a more advance baseline BEVerse [40], NeMO also improves the per timestamp perception mIoU

Table 2: Experiments of BEV stitching and temporal fusion methods in multi-frame grid fusion to generate long-range maps, for both single front view (*fcam*) and six surrounding image (*6cam*).

<i>fcam</i>	Single-frame PV-to-BEV	Multi-frame Grid Fusion	mIoU(%)			
			Divider	Ped Crossing	Boundary	All
Nus	HDMaNet	Overwrite	40.7	13.5	36.4	30.2
		Maxpool	42.6	12.7	39.4	31.5
		NeMO	<b>47.2</b>	<b>21.6</b>	<b>44.8</b>	<b>37.9</b>
BDD	HDMaNet	Overwrite	29.9	7.0	16.4	17.8
		Maxpool	26.2	4.7	14.9	13.9
		NeMO	<b>37.5</b>	<b>12.8</b>	<b>22.5</b>	<b>24.3</b>
<b><i>6cam</i></b>						
Nus	HDMaNet	Overwrite	34.4	10.0	32.1	25.6
		Maxpool	43.3	13.9	42.1	33.1
		NeMO	<b>48.7</b>	<b>29.1</b>	<b>49.7</b>	<b>42.5</b>
	BEVerse	Overwrite	52.6	28.1	49.3	43.3
		Maxpool	61.7	46.1	59.8	55.8
		NeMO	<b>62.5</b>	<b>49.5</b>	<b>61.6</b>	<b>57.9</b>

Table 3: Experiments of NeMO (a) w/ and w/o LSA fine spatial matching, (b) different supervision types, and (c) different designs of HomoGridFusion. Results shown in the table are mIoU (%). For comparison, the first column shows the results of NeMO system with LSA model, many-to-one supervision, and has 2d convolutional layers in HomoGridFusion.

	Baseline	NeMO	Spatial Matching	Supervision	HomoGridFusion Design	
			w/o LSA	Many-to-many	LSTM	Conv1d+LSTM
Divider	43.3	48.7	46.8	42.0	44.7	45.1
Ped Xing	13.9	29.1	27.9	20.0	20.7	22.0
Boundary	42.1	49.7	46.2	42.5	44.8	43.9
All	33.1	42.5	40.3	34.9	36.8	37.0

from 49.8 to 54.4. It is worth mentioning that NeMO only introduce a minor increase in model size, meaning that NeMO has potential of obtaining considerable advantages at an inconsequential cost.<sup>4</sup>

We also generate big local map for each scene (150 scenes in NuScenes and 46 scenes in BDD-Map) and evaluate the scene-based map segmentation performance in Table 2. The results demonstrate that NeMO leads to significantly improved accuracy of perception when compared to non-parameterized baseline techniques, across all conditions. This suggests that the proposed design of the grid-based fusion architecture and shared fusion model can effectively handle the processes of information screening, updating, and memorization involved in temporal fusion. Besides, it can be observed Maxpool outperform Overwrite in all settings except for the case of BDD *fcam*. It is due to the low accuracy of the pose in BDD-Map dataset: selecting the maximum value tends to maintain more noise data which in turn diminishes the overall accuracy.

### 5.3 Ablation Study

We conduct ablation study based on HDMaNet-NeMO using *6cam* NuScenes dataset.

**Impacts of local-spatial attention (LSA) model.** We analyze the impact of fine spatial matching LSA model in NeMO system. As shown in Table 3, NeMO with LSA model demonstrates advantages

<sup>4</sup>The reimplementation of *fcam* HDMaNet exhibits a significantly lower parameter count than its official counterpart *6cam* HDMaNet. This discrepancy can be attributed to the difference in view fusion module architecture between the two models, wherein the latter employs 6 independent MLPs for 6 surrounding camera views while the former only requires one MLP for *fcam*.



Table 4: Experiments of map generation with noisy pose information.

Noise	[0, 0]			[0.1, 0.1]			[0.5, 0.5]		
	Overwrite	Maxpool	NeMO	Overwrite	Maxpool	NeMO	Overwrite	Maxpool	NeMO
Divider	34.4	43.3	48.7	33.2	42.2	48.0	22.5	15.8	39.6
Ped Xing	10.0	13.9	29.1	9.9	13.6	28.8	8.2	8.5	26.8
Boundary	32.1	42.1	49.7	31.2	41.5	49.1	23.1	23.9	44.1
All	25.5	33.1	42.5	24.8	32.4	42.0	17.9	16.1	36.8

in all classes compared to the result without LSA. This experiment highlights the role of local-spatial fusion design in enhancing the performance of temporal fusion in map generation.

**Convolutional layers in HomoGridFusion.** For the default setting, we use 2D convolutional layers before LSTM[14] recurrent block. We compare it with two other designs in HomoGridFusion, i.e., HomoGridFusion without convolutional layers (“LSTM”) and with simple Conv1D (“conv1d+LSTM”). Table 3 shows that 2D convolutional layers lead to better performance for long-range map generation.

**Supervision types in HomoGridFusion.** The recurrent network in HomoGridFusion can be supervised in various ways. Many-to-many supervision is implemented by conducting supervision to partial grids at each timestamp, while many-to-one supervision applies clip-based map-wide supervision to all grids evolved. Results in Table 3 demonstrate that many-to-one supervision surpasses the performance of many-to-many method, suggesting that many-to-one supervision enables the model to learn to effectively disregard and memorize information across multiple frames in a more global sense. Such an approach is particularly beneficial for NeMO’s map generation process.

**Impacts of pose noises.** We validate NeMO’s capability in handling noisy pose information through experiments on the BDD-Map dataset in Table 1 and Table 2. Besides, we manually introduce pose noises in the NuScenes dataset and compare NeMO with baselines across two noise levels. In Table 4, we show results of Gaussian noise added to ego pose with different standard deviation. Specifically, [0.5, 0.5] represents a random  $e \in N(0, 0.5)$  degree is added to each of three Euler angles in R, and  $e \in N(0, 0.5)$  meters of noise are added to the x and y coordinates in T. It can be observed that, as the pose noise increases, the performance of long-range maps generated via overwriting and maxpooling substantially deteriorates. Despite a slight reduction, NeMO exhibits a relatively high level of performance. Notably, even with a 0.5 noise level present, NeMO outperforms the noise-free maxpool method, demonstrating its considerable capability to tackle noisy poses.

## 6 Conclusion and Discussion

**Conclusion.** This paper presents a novel neural map growing system, named NeMO. By employing coarse-to-fine spatial matching and HomoGridFusion module to fuse temporal information, NeMO generates long-range segmentation maps of target areas from image streams. Experiments demonstrate that, with model size increase a little for temporal fusion, NeMO leads to a significant improvement in the generated Bird’s-Eye-View (BEV) map compared to other existing methods. Besides, we evaluate the performance of long-range local maps generated from all images in each scene and provide a benchmark within this novel evaluation framework. We show that NeMO achieves broad generalization across scenes and various sizes of BEV plane. Meanwhile, we extend a portion of BDD100K dataset by incorporating BEV map element annotations and release BDD-Map as a new BEV dataset. We hope to provide a comprehensive and diverse resource to facilitate further advancement in the field of related research.

**Broader impacts.** The study suggests that employing a shared, grid-based, and location- and view-independent fusion network to temporally fuse individual BEV grids in a big feature map yields significant improvements. Instead of fusing temporal BEV maps in ego coordinate system, it extracts, denoises, memorizes, and updates map information in real space, which redefine the paradigm of temporal fusion. We release a BDD-Map dataset and tools for generating BEV annotations to aid others in producing more diverse BEV datasets. We hope these initial exploratory undertakings and related resources will advance BEV perception.

**Limitations and future directions.** One of the limitations of this study is evident in the implementation aspect. While NeMO framework supports end-to-end training, a two-stage approach is employed

in this study, whereby the single-frame PV-to-BEV perception model and the multi-frame fusion model are separately trained and supervised. As a result, the ultimate fusion outcome is notably constrained by the initial PV-to-BEV model, limiting its performance and effectiveness. Therefore, a potential avenue for future research is to investigate methodologies for end-to-end training.

## References

- [1] Tesla ai day 2021. <https://www.youtube.com/watch?v=j0z4FweCy4M>. Accessed: 2023-05-12.
- [2] Syed Ammar Abbas and Andrew Zisserman. A geometric approach to obtain a bird’s eye view from an image. In *Proceedings of the IEEE/CVF International Conference on Computer Vision Workshops*, pages 0–0, 2019.
- [3] Florent Bartoccioni, Éloi Zablocki, Andrei Bursuc, Patrick Pérez, Matthieu Cord, and Karteek Alahari. Lara: Latents and rays for multi-camera bird’s-eye-view semantic segmentation. In *Conference on Robot Learning*, pages 1663–1672. PMLR, 2023.
- [4] Holger Caesar, Varun Bankiti, Alex H Lang, Sourabh Vora, Venice Erin Liong, Qiang Xu, Anush Krishnan, Yu Pan, Giancarlo Baldan, and Oscar Beijbom. nuscenes: A multimodal dataset for autonomous driving. In *Proceedings of the IEEE/CVF conference on computer vision and pattern recognition*, pages 11621–11631, 2020.
- [5] Yigit Baran Can, Alexander Liniger, Danda Pani Paudel, and Luc Van Gool. Structured bird’s-eye-view traffic scene understanding from onboard images. In *Proceedings of the IEEE/CVF International Conference on Computer Vision*, pages 15661–15670, 2021.
- [6] Yigit Baran Can, Alexander Liniger, Ozan Unal, Danda Paudel, and Luc Van Gool. Understanding bird’s-eye view of road semantics using an onboard camera. *IEEE Robotics and Automation Letters*, 7(2):3302–3309, 2022.
- [7] Li Chen, Chonghao Sima, Yang Li, Zehan Zheng, Jiajie Xu, Xiangwei Geng, Hongyang Li, Conghui He, Jianping Shi, Yu Qiao, et al. Persformer: 3d lane detection via perspective transformer and the openlane benchmark. In *Computer Vision–ECCV 2022: 17th European Conference, Tel Aviv, Israel, October 23–27, 2022, Proceedings, Part XXXVIII*, pages 550–567. Springer, 2022.
- [8] Shaoyu Chen, Tianheng Cheng, Xinggang Wang, Wenming Meng, Qian Zhang, and Wenyu Liu. Efficient and robust 2d-to-bev representation learning via geometry-guided kernel transformer. *arXiv preprint arXiv:2206.04584*, 2022.
- [9] Noa Garnett, Rafi Cohen, Tomer Pe’er, Roei Lahav, and Dan Levi. 3d-lanenet: end-to-end 3d multiple lane detection. In *Proceedings of the IEEE/CVF International Conference on Computer Vision*, pages 2921–2930, 2019.
- [10] Shi Gong, Xiaoqing Ye, Xiao Tan, Jingdong Wang, Errui Ding, Yu Zhou, and Xiang Bai. Gitnet: Geometric prior-based transformation for birds-eye-view segmentation. In *Computer Vision–ECCV 2022: 17th European Conference, Tel Aviv, Israel, October 23–27, 2022, Proceedings, Part I*, pages 396–411. Springer, 2022.
- [11] Nikhil Gosala and Abhinav Valada. Bird’s-eye-view panoptic segmentation using monocular frontal view images. *IEEE Robotics and Automation Letters*, 7(2):1968–1975, 2022.
- [12] Yuliang Guo, Guang Chen, Peitao Zhao, Weide Zhang, Jinghao Miao, Jingao Wang, and Tae Eun Choe. Gen-lanenet: A generalized and scalable approach for 3d lane detection. In *Computer Vision–ECCV 2020: 16th European Conference, Glasgow, UK, August 23–28, 2020, Proceedings, Part XXI 16*, pages 666–681. Springer, 2020.
- [13] Noureldin Hendy, Cooper Sloan, Feng Tian, Pengfei Duan, Nick Charchut, Yuesong Xie, Chuang Wang, and James Philbin. Fishing net: Future inference of semantic heatmaps in grids. *arXiv preprint arXiv:2006.09917*, 2020.
- [14] Sepp Hochreiter and Jürgen Schmidhuber. Long short-term memory. *Neural computation*, 9(8):1735–1780, 1997.
- [15] Anthony Hu, Zak Murez, Nikhil Mohan, Sofía Dudas, Jeffrey Hawke, Vijay Badrinarayanan, Roberto Cipolla, and Alex Kendall. Fiery: future instance prediction in bird’s-eye view from surround monocular cameras. In *Proceedings of the IEEE/CVF International Conference on Computer Vision*, pages 15273–15282, 2021.

- [16] Junjie Huang and Guan Huang. Bevdet4d: Exploit temporal cues in multi-camera 3d object detection. *arXiv preprint arXiv:2203.17054*, 2022.
- [17] Yanqin Jiang, Li Zhang, Zhenwei Miao, Xi Tian Zhu, Jin Gao, Weiming Hu, and Yu-Gang Jiang. Polarformer: Multi-camera 3d object detection with polar transformers. *arXiv preprint arXiv:2206.15398*, 2022.
- [18] Diederik P Kingma and Jimmy Ba. Adam: A method for stochastic optimization. *arXiv preprint arXiv:1412.6980*, 2014.
- [19] Qi Li, Yue Wang, Yilun Wang, and Hang Zhao. Hdmapnet: An online hd map construction and evaluation framework. In *2022 International Conference on Robotics and Automation (ICRA)*, pages 4628–4634. IEEE, 2022.
- [20] Zhiqi Li, Wenhai Wang, Hongyang Li, Enze Xie, Chonghao Sima, Tong Lu, Yu Qiao, and Jifeng Dai. Bevformer: Learning bird’s-eye-view representation from multi-camera images via spatiotemporal transformers. In *Computer Vision–ECCV 2022: 17th European Conference, Tel Aviv, Israel, October 23–27, 2022, Proceedings, Part IX*, pages 1–18. Springer, 2022.
- [21] Yingfei Liu, Tiancai Wang, Xiangyu Zhang, and Jian Sun. Petr: Position embedding transformation for multi-view 3d object detection. In *Computer Vision–ECCV 2022: 17th European Conference, Tel Aviv, Israel, October 23–27, 2022, Proceedings, Part XXVII*, pages 531–548. Springer, 2022.
- [22] Yingfei Liu, Junjie Yan, Fan Jia, Shuailin Li, Qi Gao, Tiancai Wang, Xiangyu Zhang, and Jian Sun. Petr2: A unified framework for 3d perception from multi-camera images. *arXiv preprint arXiv:2206.01256*, 2022.
- [23] Chenyang Lu, Marinus Jacobus Gerardus van de Molengraft, and Gijs Dubbelman. Monocular semantic occupancy grid mapping with convolutional variational encoder–decoder networks. *IEEE Robotics and Automation Letters*, 4(2):445–452, 2019.
- [24] Hanspeter A Mallot, Heinrich H Bülthoff, JJ Little, and Stefan Bohrer. Inverse perspective mapping simplifies optical flow computation and obstacle detection. *Biological cybernetics*, 64(3):177–185, 1991.
- [25] Kaustubh Mani, Swapnil Daga, Shubhika Garg, Sai Shankar Narasimhan, Madhava Krishna, and Krishna Murthy Jatavallabhula. Monolayout: Amodal scene layout from a single image. In *Proceedings of the IEEE/CVF Winter Conference on Applications of Computer Vision*, pages 1689–1697, 2020.
- [26] Lang Peng, Zhirong Chen, Zhangjie Fu, Pengpeng Liang, and Erkang Cheng. Bevsegformer: Bird’s eye view semantic segmentation from arbitrary camera rigs. In *Proceedings of the IEEE/CVF Winter Conference on Applications of Computer Vision*, pages 5935–5943, 2023.
- [27] Jonah Philion and Sanja Fidler. Lift, splat, shoot: Encoding images from arbitrary camera rigs by implicitly unprojecting to 3d. In *Computer Vision–ECCV 2020: 16th European Conference, Glasgow, UK, August 23–28, 2020, Proceedings, Part XIV 16*, pages 194–210. Springer, 2020.
- [28] Zequn Qin, Jingyu Chen, Chao Chen, Xiaozhi Chen, and Xi Li. Uniformer: Unified multi-view fusion transformer for spatial-temporal representation in bird’s-eye-view. *arXiv preprint arXiv:2207.08536*, 2022.
- [29] Cody Reading, Ali Harakeh, Julia Chae, and Steven L Waslander. Categorical depth distribution network for monocular 3d object detection. In *Proceedings of the IEEE/CVF Conference on Computer Vision and Pattern Recognition*, pages 8555–8564, 2021.
- [30] Lennart Reiher, Bastian Lampe, and Lutz Eckstein. A sim2real deep learning approach for the transformation of images from multiple vehicle-mounted cameras to a semantically segmented image in bird’s eye view. In *2020 IEEE 23rd International Conference on Intelligent Transportation Systems (ITSC)*, pages 1–7. IEEE, 2020.
- [31] Thomas Roddick and Roberto Cipolla. Predicting semantic map representations from images using pyramid occupancy networks. In *Proceedings of the IEEE/CVF Conference on Computer Vision and Pattern Recognition*, pages 11138–11147, 2020.
- [32] Thomas Roddick, Alex Kendall, and Roberto Cipolla. Orthographic feature transform for monocular 3d object detection. *arXiv preprint arXiv:1811.08188*, 2018.
- [33] Bryan C Russell, Antonio Torralba, Kevin P Murphy, and William T Freeman. Labelme: a database and web-based tool for image. *Int. J. of Computer Vision*, 77(1), 2005.

- [34] Avishkar Saha, Oscar Mendez, Chris Russell, and Richard Bowden. Translating images into maps. In *2022 International Conference on Robotics and Automation (ICRA)*, pages 9200–9206. IEEE, 2022.
- [35] Ruihao Wang, Jian Qin, Kaiying Li, Yaochen Li, Dong Cao, and Jintao Xu. Bev-lanedet: a simple and effective 3d lane detection baseline, 2023.
- [36] Yue Wang, Vitor Campagnolo Guizilini, Tianyuan Zhang, Yilun Wang, Hang Zhao, and Justin Solomon. Detr3d: 3d object detection from multi-view images via 3d-to-2d queries. In *Conference on Robot Learning*, pages 180–191. PMLR, 2022.
- [37] Xuan Xiong, Yicheng Liu, Tianyuan Yuan, Yue Wang, Yilun Wang, and Hang Zhao. Neural map prior for autonomous driving. In *Proceedings of the IEEE/CVF Conference on Computer Vision and Pattern Recognition*, pages 17535–17544, 2023.
- [38] Weixiang Yang, Qi Li, Wenxi Liu, Yuanlong Yu, Yuexin Ma, Shengfeng He, and Jia Pan. Projecting your view attentively: Monocular road scene layout estimation via cross-view transformation. In *Proceedings of the IEEE/CVF Conference on Computer Vision and Pattern Recognition*, pages 15536–15545, 2021.
- [39] Fisher Yu, Haofeng Chen, Xin Wang, Wenqi Xian, Yingying Chen, Fangchen Liu, Vashisht Madhavan, and Trevor Darrell. Bdd100k: A diverse driving dataset for heterogeneous multitask learning. In *Proceedings of the IEEE/CVF conference on computer vision and pattern recognition*, pages 2636–2645, 2020.
- [40] Yunpeng Zhang, Zheng Zhu, Wenzhao Zheng, Junjie Huang, Guan Huang, Jie Zhou, and Jiwen Lu. Beverse: Unified perception and prediction in birds-eye-view for vision-centric autonomous driving. *arXiv preprint arXiv:2205.09743*, 2022.
- [41] Brady Zhou and Philipp Krähenbühl. Cross-view transformers for real-time map-view semantic segmentation. In *Proceedings of the IEEE/CVF Conference on Computer Vision and Pattern Recognition*, pages 13760–13769, 2022.
- [42] Xizhou Zhu, Weijie Su, Lewei Lu, Bin Li, Xiaogang Wang, and Jifeng Dai. Deformable detr: Deformable transformers for end-to-end object detection. *arXiv preprint arXiv:2010.04159*, 2020.

## A Appendix

### A.1 Implementation Details

The workflow of the NeMO system incorporates three stages: PV-to-BEV feature transformation, coarse-to-fine spatial matching, and temporal fusion with HomoGridFusion. Corresponding PV-to-BEV and spatial matching & temporal fusion sub-networks may be subject to end-to-end training or separate training. This paper follows the latter scheme and present details regarding the implementation of training and inference. The system and models we employ in this study are designed for semantic segmentation task, aiming to recognize three static map elements: lane divider, pedestrian crossing, and boundary.

#### A.1.1 Training phase

The data loaders used for PV-to-BEV model and spatial matching & temporal fusion model (LSA and HomoGridFusion) are different as the latter requires time-series image sequence rather than single frame image. In the case of PV-to-BEV model, each sample consists of images obtained at one timestamp. The PV-to-BEV model itself is trained in an end-to-end manner. We omit relevant descriptions as we conduct the same operations as elaborated in corresponding studies, e.g., HDMapNet[19] and BEVFormer[40] in the current work. In the following, we focus on HDMapNet-based NeMO with *6cam* input and provide more implementation details in practice.

**Clip data preparation.** For LSA and HomoGridFusion network, a sample from data loader is composed of a clip created with a sequence of  $T = 4$  consecutive frames, and a batch has  $B$  4-frame clips in total. Batch size  $B \in \{1, 2, 4, 8\}$  is adjustable in distributed training. For instance, we use  $B = 8$  when training with 8 GPUs. In each clip, each image  $\mathcal{I}_t$  is first converted to  $\mathcal{F}_t^{bev} \subseteq \mathbb{R}_{O_e}^{200 \times 400 \times 4}$ ,  $t \in \{1, 2, \dots, T\}$ , via the trained PV-to-BEV model HDMapNet. Here HDMapNet is

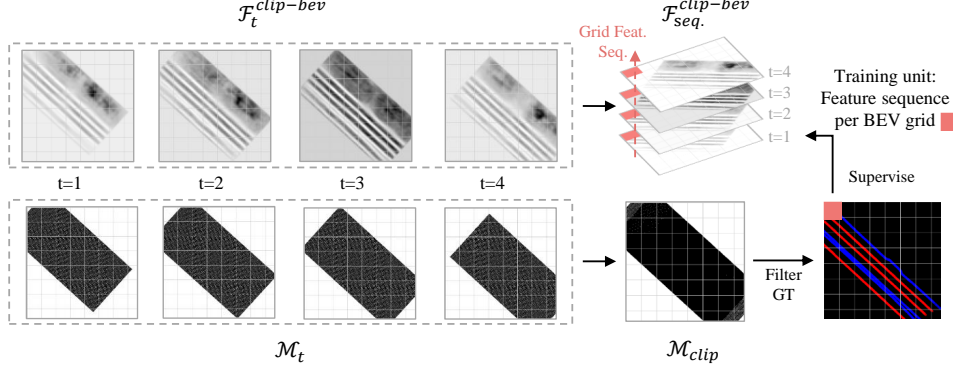


Figure 6: Temporal fusion model training sample generation process.

in evaluation mode and the parameters are not updated in the process. While  $\mathcal{F}_t^{bev}$  can be BEV features obtained at any stage in the PV-to-BEV network, we use the features returned by semantic HDMapNet decoder as  $\mathcal{F}_t^{bev} \subseteq \mathbb{R}_{O_e}^{200 \times 400 \times 4}$  in ego-centric coordinate  $O_e$ .

For each clip, we restrict the spatial range of interest in  $O_g$  by defining a big BEV plane  $\mathcal{F}_{clip}^{bev} \subseteq \mathbb{R}_{O_g}^{384 \times 384 \times 4}$  functioning as the big BEV feature map. At each timestamp  $t \in \{1, 2, 3, 4\}$ , ego-centric  $\mathcal{F}_t^{bev} \subseteq \mathbb{R}_{O_e}^{200 \times 400 \times 4}$  can be mapped to generate  $\mathcal{F}_t^{clip-bev} \subseteq \mathbb{R}_{O_g}^{384 \times 384 \times 4}$  with ego pose  $E_t$  (see four  $\mathcal{F}_t^{clip-bev}$  figures in Figure 6). Meanwhile, we generate masks  $\mathcal{M}_t$  corresponding to the mapped location in the big BEV plane for loss calculation.

**Fine spatial matching.** During NeMO experimental trials conducted without LSA architecture (Section 5.3 and Table 3), the sequence  $\mathcal{F}_T^{clip-bev}$  is directly fed to temporal fusion (HomoGridFusion) model as shown in Figure 6. When incorporating fine spatial matching, we add a local-spatial attention structure as we described in Section 3.1 at this stage. For timestamp  $t \in \{2, 3, 4\}$ , the better aligned features  $\mathcal{F}_{t,cur}^{bev}$  returned from LSA, instead of the original  $\mathcal{F}_{t,cur}^{bev}$ , are converted to big BEV plane with ego pose  $E_t$  to obtain  $\mathcal{F}_t^{clip-bev}$ .

Besides, Gaussian blurring or linear interpolation can be added to  $\mathcal{F}_t^{bev}$  for smoothing. In practice, we use Gaussian blurring (with kernel size 7 and sigma 5) considering the processing time.

**Temporal fusion with HomoGridFusion.** As shown in Figure 6, all four  $\mathcal{F}_t^{clip-bev}$  in each clip can form a temporal sequence of BEV features  $\mathcal{F}_{seq}^{clip-bev} \subseteq \mathbb{R}_{O_g}^{B \times 4 \times 384 \times 384 \times 4}$ . In one clip, each grid in the big BEV plane, denoted by  $\mathcal{F}_{seq}^{clip-bev}[h][w]$ , is a sequence of 4 historical BEV features. For HomoGridFusion structure, grid feature sequence is the sample unit for training, and a  $\mathcal{F}_{seq}^{clip-bev}$  has  $384 \times 384$  sample units. We illustrate one grid feature sequence in Figure 6 with pink squares. The ground truth  $\mathcal{F}_{GT} \subseteq \mathbb{R}^{B \times 384 \times 384 \times 4}$  is first cropped according to the global location and area of  $\mathcal{F}_{seq}^{clip-bev}$ , and then filtered with the assistance of mask  $\mathcal{M}_{clip}$  generated by combining all  $\mathcal{M}_t$ s. In each clip, the corresponding ground truth grid  $\mathcal{F}_{GT}[h][w]$  is used to supervise sample unit  $\mathcal{F}_{seq}^{clip-bev}[h][w]$  in HomoGridFusion.

In practice, we first add three  $3 \times 3$  convolutional layers to  $\mathcal{F}_{seq}^{clip-bev}$  with strides of 1 and output channels of 64, 128, 256. The first two convolutional layers are followed by ReLU and  $3 \times 3$  maxpooling layers with strides of 1 and paddings of 1, and the last convolutional layer followed by batch normalization and ReLU. The outcome of the convolutional layers  $\mathcal{F}_{seq}^{clip-bev}$  has a shape of  $B \times 4 \times 384 \times 384 \times 256$ , where  $B$  is batch size, 4 is sequence length, and 256 is feature channels. We adopt two bidirectional LSTM followed by two MLP structures for grid-based feature sequence fusion in HomoGridFusion. For LSTM training, the  $\mathcal{F}_{seq}^{clip-bev}$  is unfolded to generate  $B \times 384 \times 384$  feature sequences. The input batch size of the model was configured to be  $B \times 384 \times 384$ , while the sequence length and number of feature channels are set to 4 and 256, respectively. In LSTM temporal fusion, we reduce the resultant output feature channels back to 4. With many-to-one strategy, we use  $\mathcal{F}_{GT}$  to supervise the grid features in the last sequence layer of LSTM outcomes.

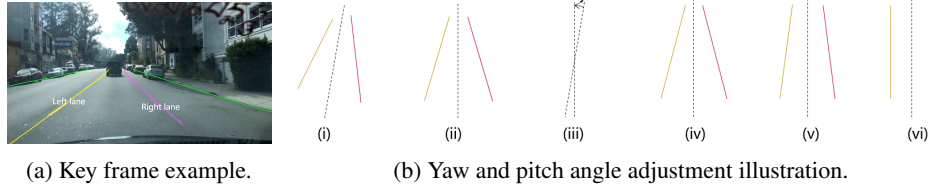


Figure 7: BDD-Map clip-level extrinsic adjustment.

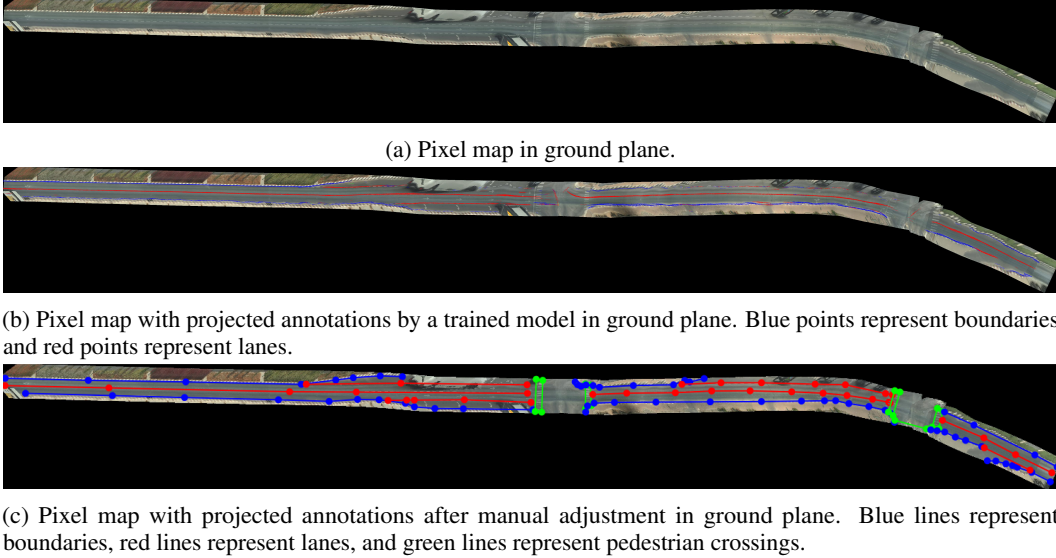


Figure 8: Semi-automated BEV annotation generation of one clip.

### A.1.2 Inference phase

The inference process is similar to the procedure shown in Figure 1. In inference phase, we first define an all-zero initial  $\mathcal{F}_{map}^{bev} \subseteq \mathbb{R}_{O_g}^{H_{bev}^{map} \times W_{bev}^{map} \times K}$  representing the big feature map.

We process each frame in a scene in chronological order. For each frame at timestamp  $t$ ,  $\mathcal{I}_t$  is converted to  $\mathcal{F}_{cur}^{bev} \subseteq \mathbb{R}_{O_e}^{200 \times 400 \times 4}$ . We conduct coarse spatial matching to obtain historical BEV  $\mathcal{F}_{hist}^{bev} \subseteq \mathbb{R}_{O_e}^{200 \times 400 \times 4}$  by sampling from  $\mathcal{F}_{map}^{bev}$  according to ego pose  $E_t$ , and fine spatial matching to obtain  $\tilde{\mathcal{F}}_{cur}^{bev} \subseteq \mathbb{R}_{O_e}^{200 \times 400 \times 4}$  with LSA model.  $\tilde{\mathcal{F}}_{cur}^{bev}$  and  $\mathcal{F}_{hist}^{bev}$  are temporally fused with HomoGridFusion to obtain  $\mathcal{F}_{fused}^{bev}$ , which is further used to update corresponding grids in the big feature map  $\mathcal{F}_{map}^{bev}$ .

Finally, for evaluation, we use one hot encoding to convert  $\mathcal{F}_{map}^{bev}$  to long-range local map.

## A.2 BDD-Map Annotation Pipeline

For each 40s clip, BDD100K provides a rough trajectory in 1 Hz. It is interpolated into 30Hz and subsequently every frame in the clip video is assigned a rough pose based on the trajectory. Videos in BDD100K are captured by iPhone 5 with 720p videos, and therefore we approximate intrinsic parameters based on focal length 700px and assume no distortion. To address the variability of unrestricted phone placements by drivers, we propose a pipeline for estimating extrinsic parameters, which may differ from clip to clip.

Based on the observation that phone is not likely repositioned significantly within one clip, we use a constant extrinsic matrix for each clip. To begin, we utilize a well-trained PV lane detection model to extract the lanes and boundaries within each frame of the video. From there, we select key frames that have two clearly detected lane lines on both sides of the ego car, left lane and right lane as shown

in Figure 7a. Assuming that the lane lines on both sides of the lane in which the car is traveling are parallel, we adjust the pitch and yaw angles in the extrinsic parameters until the lane lines on both sides of the vehicle in BEV are parallel, and we assume a roll angle of zero for all clips based on the observed vertical stability of the scene in the videos. We first initialize pitch and yaw as zeros, and cast the left and right lane into BEV. Due to yaw angle, two parallel lanes in BEV are not symmetric about a vertical axis as shown in Figure 7b(i). We calculate the axis of symmetry for the two lanes in BEV, and rotate it to align with the vertical axis (Figure 7b(ii)). The resulting angle of rotation is referred to as the yaw angle (Figure 7b(iii)). We then adjust the pitch angle iteratively to make the symmetric lanes parallel to the vertical axis as shown in Figure 7b(v) and Figure 7b(vi).

With ego poses per frame, constant intrinsic matrix and optimized extrinsic matrix, we construct the ground plane pixel map with Inverse Perspective Mapping (IPM) algorithm. For overlapping area, pixels are overwritten by the most recent frame. Meanwhile, road elements extracted by a model are transformed to the ground plane as shown in Figure 8b. The road elements related points are filtered and vectorized into instance level lanes and boundaries as shown in Figure 8c.

To ensure accuracy, the final annotated results are subjected to human inspection and adjustments, and pedestrian crossings are manually added to the annotations. In order to facilitate human inspection and provide additional information that may not be clear in the BEV, we have developed a special command based on LabelMe[33]. When a user right-clicks on a point in the pixel map, the corresponding image will appear for further inspection.

### A.3 Visualization of Experimental Results in NuScenes and BDD-Map

In Figure 9 we provide more visualization results of scene-level long-range map on NuScenes dataset. It can be observed that NeMO surpasses two baselines by comprehensively capturing road elements while retaining more details, particularly in intersections. Notably, NeMO excels in capturing essential road structure information in complex scenes despite some noises in the generated map, as demonstrated in the final two cases in Figure 9. The overwriting and maxpooling techniques lead to comparatively poor performance primarily due to lower perception accuracy for elements at far distances compared to that of near ones in single-frame perception. As a result, during the time series update, there is a risk that higher accuracy perception results obtained at an earlier time may be overwritten and replaced by inferior results obtained later as the vehicle moves forward. Our method, however, addresses this issue by utilizing neural networks for effective information selection and update to better preserve accuracy over time.

Figure 10 and Figure 11 are visualizations of cases in BDD-Map dataset. In contrast to NuScenes, BDD-Map has more frames in scene clips and correspondingly longer-range local maps. NeMO paradigm proves highly effective in the creation of road structures in both straight road scenes (Figure 10) and turning scenes (Figure 11). These results indicate the continued viability of NeMO even in scenarios with less accurate sensor readings, underscoring its practical utility across a wide range of applications. Another observation is that in BDD-Map scenes, overwriting tends to outperform maxpooling approach. A possible explanation for this outcome is that the maxpooling approach that conserves maximum values can be more significantly influenced by pose noises. Specifically, multiple feature channels may retain large values in temporal update process, thus reducing the capacity of discrimination for key information.



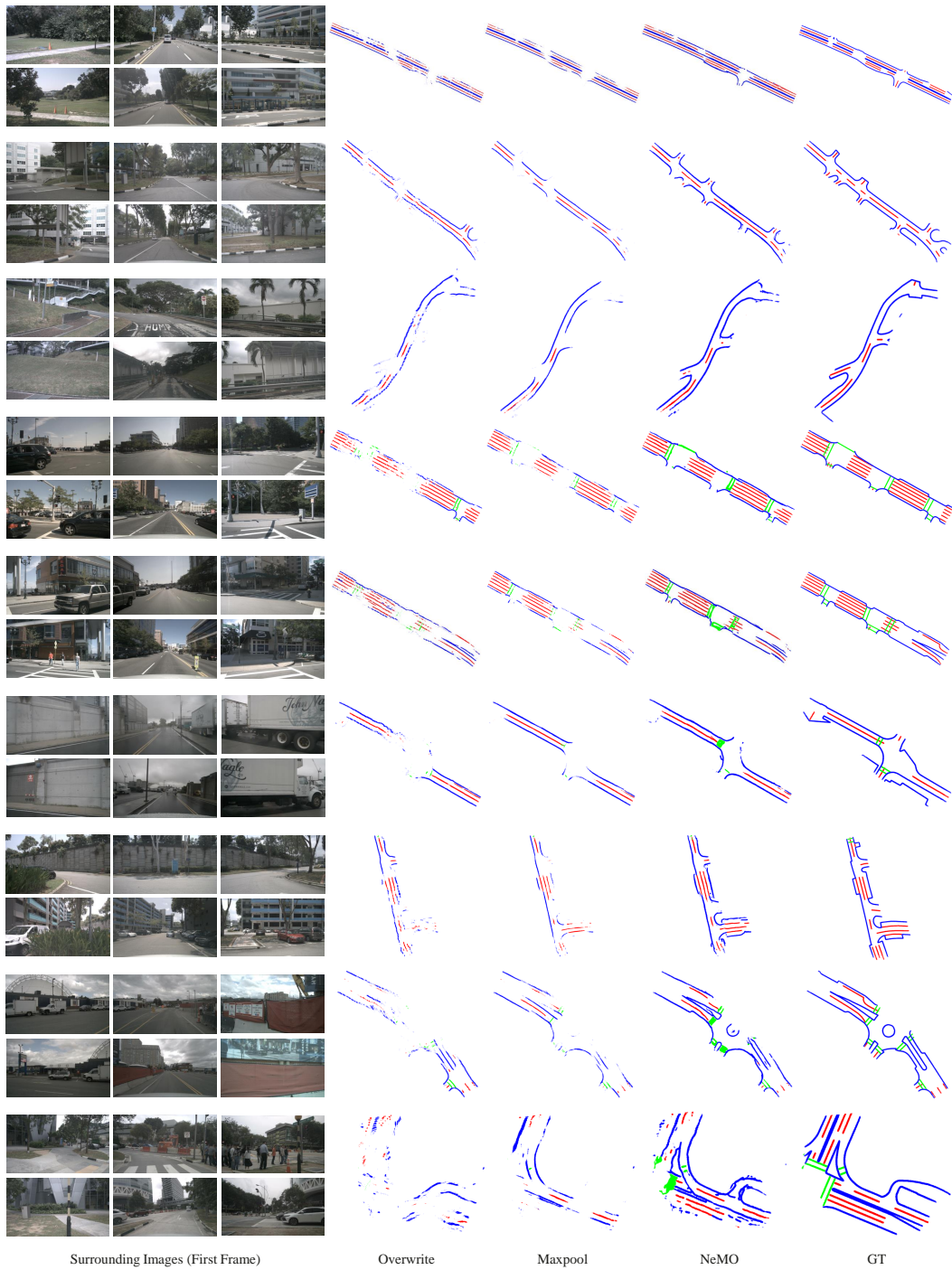


Figure 9: Visual comparison on NuScenes scene-level long-range map generation.

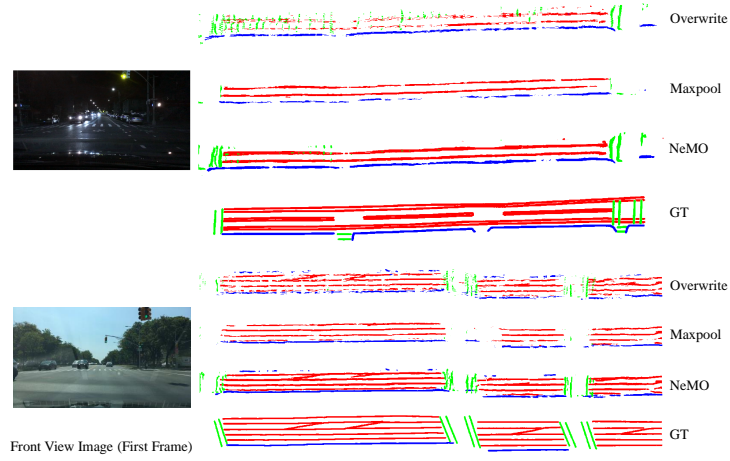


Figure 10: Visual comparison on BDD-Map scene-level long-range map generation (straight lanes).

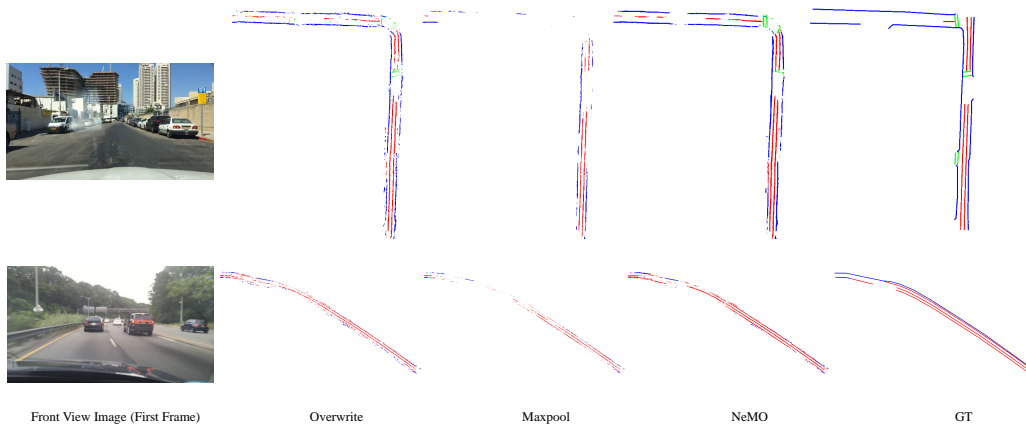


Figure 11: Visual comparison on BDD-Map scene-level long-range map generation (turning and curving).